Graphene plasmonic skyrmion lattices generated by radially polarized light beams

Lei Wang [*], Lixin Ge, and Ke Gong

College of Physics and Electronic Engineering, Xinyang Normal University, Xinyang 464000, China

Wei Cai,[†] Xinzheng Zhang, and Jingjun Xu[‡]

The Key Laboratory of Weak-Light Nonlinear Photonics, Ministry of Education, School of Physics and TEDA Applied Physics Institute, Nankai University, Tianjin 300457, China

Topological quasiparticles with sophisticated vectorial structures such as skyrmions play a key role in a variety of physical systems, ranging from quantum fields to magnetic materials. Wherein, optical skyrmions have attracted great attention due to their potential applications in optical information processing, transfer, and storage. In this paper, tunable plasmonic skyrmion lattices are demonstrated on graphene surfaces, where the graphene plasmons are excited using three pairs of dielectric diffractive gratings with radially polarized light beams. We have found that graphene plasmonic skyrmions with identical field distributions at different excited wavelengths can be achieved by tuning the Fermi energies without reoptimizing the grating structures, and the unit cell size of graphene plasmonic skyrmion lattices can also be actively tuned by Fermi energies at fixed excitation frequencies. Moreover, synthesized doughnut right-circularly polarized beams can also excite the plasmonic skyrmions in the axial symmetric structure with half the excitation efficiency compared to radially polarized beams. The proposed devices may find applications in optical information storage and manipulation in a chip.

I. INTRODUCTION

Skyrmions, the generalized topological quasiparticle models proposed by Skyrme [1], have been considered in many platforms [2]. Over the last decades, magnetic skyrmions have attracted enormous research interest, due to their nontrivial real-space spin-swirls topologically stabilized at magnetic fields [3]. The ultracompact size and unique topological protection properties make magnetic skyrmions fundamentally interesting and technological in topological spintronics, energy-efficient data storage, and manipulation [4,5]. Very recently, skyrmionic structures have been observed in optics [6]. Tsesses *et al.* [7] have shown that optical skyrmion lattices can be generated using standing waves composed of evanescent electromagnetic fields. Davis *et al.* [8] have demonstrated time-resolved vector imaging of plasmonic skyrmions lattices with subfemtosecond time steps and a 10-nm spatial scale. Du *et al.* [9] have demonstrated that spin-skyrmions can be generated in the surface plasmon field in the presence of spin-orbit coupling and the local spin direction in the skyrmion-like structure can vary on the deep-subwavelength scale. Shen *et al.* [10] have demonstrated that supertoroidal pulses also exhibit skyrmionic structure of the electromagnetic fields. In addition to the Néel-type photonic skyrmions, Bloch-type photonic skyrmions have been proposed in optical chiral mul-

tilayers [11,12], and the characterized topological structures of bimeron (the quasiparticle homeomorphic to skyrmion) have also been proposed in free space with Néel, Bloch, and anti-skyrmion types [13]. Over the last year, Liu *et al.* [14] have theoretically illustrated that vectorial holograms can be used to generate optical skyrmions with different topological features at will, and Shen *et al.* [15] have experimentally implemented a digital hologram system to generate the tunable optical skyrmions. However, the manipulation of optical skyrmions by designing different spatial structures based on noble metal is too rigid to realize device integration. Besides, the plasmonic response of noble metal is mainly in the visible to near infrared range, and thus it is difficult to realize midinfrared and terahertz applications. Moreover, due to the weak confinement of surface plasmons existed at the interface between the air and a conductor, the unit cell of the optical skyrmions lattices is in the dimensions of the wavelength scale, which has greatly limited the applications of optical skyrmions in ultracompact on-chip storage applications.

Graphene plasmons (GPs), the intrinsic collective excitations propagating along graphene sheets, have attracted much attention due to their highly tunable, extreme electromagnetic field confinement as well as long plasmonic lifetime [16–18]. Because of the unusually short wavelength relative to the free light, GPs can be utilized for enhancing light-matter interactions at deep-subwavelength scales in the midinfrared to terahertz range. In recent years, plenty of graphene-based plasmonic devices with unique properties have been proposed theoretically and demonstrated experimentally, such as photodetectors [19], biosensors [20,21], resonators [22–24],

[*]nkwanglei@mail.nankai.edu.cn

[†]weicai@nankai.edu.cn

[‡]jjxu@nankai.edu.cn

perfect absorbers [25,26], and terahertz lasers [27,28]. In the midinfrared and terahertz regime, one can expect that the deep-subwavelength tunable graphene plasmonic skyrmion lattices would exist in graphene sheets. Noticing that the optical skyrmion lattices can be regarded as coherent superposition of six symmetric transverse-magnetic evanescent guided waves [7], the key point for exciting the graphene plasmonic skyrmions is to generate three pairs of collimated in-phase propagating graphene plasmons with equal amplitudes and designated propagation directions simultaneously [7]. When using the grating excitation configuration, the incident polarization must be along the periodic direction of the gratings. However, due to the three pairs of gratings having different periodic directions, the polarization of incident light must possess cylindrical symmetry. Normally, an incident wave with spatially homogeneous states of polarization, e.g., circularly polarized beams (CPBs), was adopted to generate the surface plasmon polaritons [7,8]. However, the plasmonic skyrmions excitation with CPBs possesses two obvious disadvantages. First, CPBs will introduce extra phase difference between different gratings, demanding the wavelength-dependent displacement of the gratings to compensate for the phase difference [7,29]. As a result, each spatial structure only supports a single wavelength, which greatly weakens the advantage of the tunability of graphene plasmons. Next, the azimuthal electric field component is wasted in the excitation process, which has halved the excitation efficiency. To solve the problems, cylindrical vector beams (CVBs), specifically, radially polarized beams (RPBs), are adopted to generate the plasmonic skyrmions. CVBs are vector beam solutions of Maxwell's equations that obey axial symmetry in both amplitude and phase, and rotational symmetry in states of polarization. Wherein, the electric fields of RPBs and azimuthal polarized beams (APBs) are polarized in radial directions and azimuthal directions, respectively. RPBs have drawn much interest due to their unique features in many research fields, for example, sharp focus [30], acceleration techniques [31], particles trapping [32,33], detection and nanolocalization of dielectric particles [34], high resolution microscopy [35], and plasmonic excitation [36]. With the RPBs, one can effectively excite the graphene plasmonic skyrmion lattices without shifting the gratings.

In this paper, we report the generation of graphene plasmonic skyrmion lattices on a graphene surface with uniform Fermi energies, where the GPs are excited using dielectric diffractive gratings with phase-homogeneous radially polarized incident light beams. Graphene plasmonic skyrmions with identical field distribution at different excited frequencies can be achieved by tuning the Fermi energies, and the unit cell size of graphene plasmonic skyrmion lattice can also be tuned at fixed excited frequencies. Moreover, we analyze and compare the plasmonic skyrmions excited by synthesized doughnut radially polarized beams, azimuthal polarized
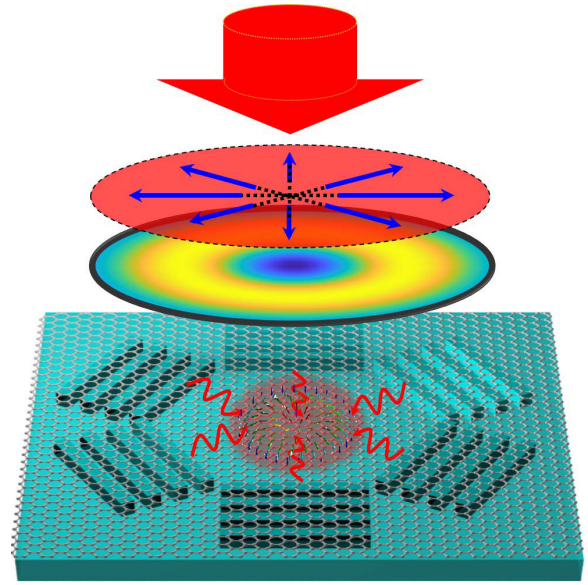

FIG. 1. Schematic diagram of the generation of optical skyrmions on the graphene surface. GPs are excited by radially polarized light with three pairs of ridged diffractive gratings and propagate toward the center of the structure to form the optical skyrmion lattice.

beams, x-polarized linearly polarized beams (LPBs), and left-circularly/right-circularly polarized beams (L-CPBs/R-CPBs), and we find that synthesized doughnut LPBs and L-CPBs cannot excite the skyrmions in our symmetric structure, due to the extra phase factor, while R-CPBs can excite the skyrmions with half the excitation efficiency compared to RPBs. Our proposed graphene plasmonic skyrmion lattice can be used for data storage and manipulation in graphene sheets in an ultracompact way.

II. THEORETICAL DESCRIPTION

The schematic diagram of the graphene plasmon skyrmions' generation is shown in Fig. 1. To couple infrared light from the air into the graphene surface waves at normal incidence, six ridged diffractive grating arrays with C_{6v} point group symmetry forming three pairs of gratings on the silica substrate are designed underneath the graphene monolayer. The duty cycle of the gratings is maintained at 0.5, and the grating arrays have the period Λ and the ridge height h_0. When the three pairs of gratings are illuminated with proper polarizations, plasmonic waves at the graphene interface with strong light confinement in the perpendicular direction can be excited, which will propagate toward the center of the structure. When the distance between the gratings and the center of the structure is L, the lossless electromagnetic field of the GPs along the x-y surface can be expressed as

$$\mathbf{E} = \begin{pmatrix} E_x^{(\omega)} \\ E_y^{(\omega)} \\ E_z^{(\omega)} \end{pmatrix} = E_0 e^{iq'L} e^{-|\kappa_z|z} \sum_{\theta=-\frac{\pi}{3},0,\frac{\pi}{3}} \begin{pmatrix} -\frac{|\kappa_z|\cos\theta}{q'}\sin[q'(x\cos\theta+y\sin\theta)] \\ -\frac{|\kappa_z|\sin\theta}{q'}\sin[q'(x\cos\theta+y\sin\theta)] \\ \cos[q'(x\cos\theta+y\sin\theta)] \end{pmatrix}, \tag{1}$$

where E_0 is a real normalization constant, $q = q' + iq''$ is the propagation constant, and thus $\lambda_p = 2\pi/q'$ denotes the GPs wavelength, $\kappa_z = \sqrt{q^2 - k_0^2}$ is the longitudinal wave number in vacuum, and $k_0 = \omega/c$ is the wave number in vacuum. It is well known that the propagation constant of a supported graphene monolayer is given by [18]

$$\frac{1}{\sqrt{k_0^2 - q^2}} + \frac{\bar{\epsilon}}{\sqrt{\bar{\epsilon}k_0^2 - q^2}} = \frac{4\pi\sigma(\omega)}{\omega}, \quad (2)$$

where $\bar{\epsilon}$ is the effective permittivity of the substrate. The complex surface conductivity σ of the graphene monolayer is governed by the Kubo formula with the random-phase approximations [37–39], which is related to the photon frequency ω, the Fermi energy E_F, the electron-phonon momentum relaxation time $\tau = \mu E_F/ev_F^2$, and the ambient temperature T:

$$\begin{aligned}
\frac{\sigma(\omega)}{\sigma_0} =& \frac{8ik_BT\ln\left[2\cosh\left(\frac{E_F}{2k_BT}\right)\right]}{\pi\hbar(\omega + i\tau^{-1})} \\
&+ \frac{\sinh\left(\frac{\hbar\omega}{2k_BT}\right)}{\cosh\left(\frac{E_F}{k_BT}\right) + \cosh\left(\frac{\hbar\omega}{2k_BT}\right)} \\
&- \frac{i}{2\pi}\ln\frac{(\hbar\omega + 2E_F)^2}{(\hbar\omega - 2E_F)^2 + (2k_BT)^2}, \quad (3)
\end{aligned}$$

where $\sigma_0 = e^2/4\hbar$, k_B is the Boltzmann constant, and $\hbar$ is the reduced Plank constant. The dimensionless conductivity can be defined as $\hat{\sigma} \equiv \frac{2\pi\sigma}{c} = \frac{\pi\alpha}{2}\frac{\sigma(\omega)}{\sigma_0}$, and $\alpha \approx 1/137$ is the fine-structure constant. Using the electrostatic limit, the propagation constant can be greatly simplified as $q/k_0 = 0.5i(1 + \bar{\epsilon})/\hat{\sigma}$. In order to effectively excite the six gratings with the same intensity, the grating period is required to satisfy the phase-matching condition

$$\frac{q'}{k_0} - \sin\theta = m\frac{\lambda}{\Lambda}, \quad (4)$$

where m is the diffraction order and θ is the incident angle. For normal incidence ($\theta = 0$) and $m = 1$, the grating period is $\Lambda = \lambda_p$. Incidentally, due to the grating geometry, the plasmon wavelength λ_p in the grating region and the free propagation region (denoted by λ_p^0) are unequal.

It is known that the transverse electric field distribution of fundamental RPBs at the beam waist $z = 0$ has the following form [40–42]:

$$\mathbf{E}_{\text{RPBs}}(x, y) = \sqrt{2}E_0^{\text{inc}}\exp\left(-\frac{\rho^2}{w_0^2}\right)\left(\frac{x}{w_0}\hat{\mathbf{e}}_x + \frac{y}{w_0}\hat{\mathbf{e}}_y\right), \quad (5)$$

where $\hat{\mathbf{e}}_x$ and $\hat{\mathbf{e}}_y$ are unit vectors in the x and y directions, respectively, $\rho = \sqrt{x^2 + y^2}$ is the radial coordinate, w_0 is the beam waist radius of the fundamental mode, and E_0^{inc} is a constant field amplitude. Noticing the associated Laguerre polynomials fulfill $L_0^1(\cdot) = 1$, the amplitude profile is exactly the Laguerre-Gauss LG_{01} mode without the vortex phase term. Moreover, the electric field of the RPBs can also be expressed as the superposition of orthogonally polarized Hermite-Gauss HG_{01} and HG_{10} modes as $\mathbf{E}_{\text{RPBs}} = \text{HG}_{10}\hat{\mathbf{e}}_x + \text{HG}_{01}\hat{\mathbf{e}}_y$. Besides, RPBs also have the advantage that the incident field intensity on the optical axis is close to zero; this will minimize the impact of the incident light on the generated skyrmion

fields, which is good for the data-acquiring process via scanning near-field optical microscopy (SNOM).

The swirling structure of a skyrmion is characterized by the topological skyrmion number defined by

$$S = \frac{1}{4\pi}\int_A \hat{\mathbf{e}} \cdot \left(\frac{\partial\hat{\mathbf{e}}}{\partial x} \times \frac{\partial\hat{\mathbf{e}}}{\partial y}\right)dA, \quad (6)$$

where the area A covers one unit cell of the lattice; $\hat{\mathbf{e}}(\mathbf{r}) = \text{Re}\{\mathbf{E}^{(\omega)}\}/|\mathbf{E}^{(\omega)}|$ is the real, normalized three-component field; and the integrand is the skyrmion number density. The skyrmion number S, being an integer, is robust to deformations of the field $\hat{\mathbf{e}}$.

III. RESULTS AND DISCUSSION

In our calculations, we start by setting the incident wavelength of the infrared light to 8.6 μm. Unless otherwise specified, the permittivity of silica at the midinfrared range is assumed to be 3.9, the grating ridge height h_0 is set as 100 nm, the graphene layer is set as the transition boundary condition with parameters $v_F = c/300$, μ = 3000 cm^2/(V s), $T = 300$ K, and $E_F = 0.65$ eV. One can find both the optimized grating period Λ and the plasmon wavelength λ_p are 305 nm in the grating region (see Appendix A), which corresponds to $\bar{\epsilon} = 2.7$ according to the simplified propagation constant formula. In the three-dimensional FEM simulation, the finite grating width and number of periods are set as 3.5 μm and six, respectively. The maximum element size in air area and silica substrate are $\lambda/6$ and $\lambda/6\sqrt{3.9}$, respectively, and the maximum element size in the graphene sheet is refined to 50 nm. Scattering boundary conditions are adopted to reduce the reflection from the boundary of the calculation window. Futhermore, the graphene sheet is modeled as a transition boundary condition with the effective bulk conductivity $\sigma(\omega)/d$, where $d \approx 0.3$ nm is the thickness of single-layer graphene. Besides, the extracted propagation constant is $q' + iq'' = (16.533 + 0.4i)k_0$ in the free propagation region, corresponding to $\lambda_p^0 = 520$ nm and $\bar{\epsilon}^0 = 1.17$, respectively; here $\bar{\epsilon}^0$ is slightly greater than the unit because $h_0 = 100$ nm is smaller than the vertical evanescent decay length of GPs. The RPBs with homogenous phase distribution are assumed to normally incident on the grating region from the air side; here we use the beam waist radius $w_0 = 7$ μm to focus the incident light into the grating regions. As a result, the calculated axial (out-of-plane) electric field E_z and the transverse (in-plane) electric field $\sqrt{E_x^2 + E_y^2}$ close to the graphene film are shown in Figs. 2(a) and 2(b). The analytical electric field without loss based on Eq. (1) is also provided in Figs. 2(d) and 2(e). The two-dimensional (2D) hexagonal lattice shown in Fig. 2 can be described by rhomboid cells. The lattice basis vectors can be expressed as $\vec{\alpha}_1 = a(\frac{\sqrt{3}}{2}, \frac{1}{2})$ and $\vec{\alpha}_2 = a(\frac{\sqrt{3}}{2}, -\frac{1}{2})$, where the lattice constant a is the distance between two adjacent antinodes. Here the Wigner-Seitz cells are extracted from the antinodes of the E_z pattern, then the unit cell area satisfies $A = |\vec{\alpha}_1 \times \vec{\alpha}_2| = \frac{\sqrt{3}}{2}a^2$. For the case of skyrmion lattices superposed by three pairs of standing waves, one has $a = \frac{2}{\sqrt{3}}\lambda_p^0$, and hence the unit cell area satisfies $A = \frac{2}{\sqrt{3}}(\lambda_p^0)^2 \approx 3.1 \times 10^5$ nm$^2 \approx 0.0042\lambda^2$. To clarify
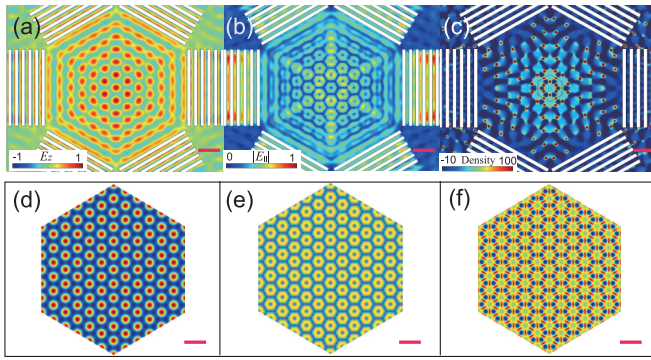
FIG. 2. Simulated optical skyrmion lattice created by GPs. (a) Real part of the axial (out-of-plane) electric field E_z. (b) Amplitude of the transverse (in-plane) electric field $\sqrt{E_x^2 + E_y^2}$. (c) Skyrmion number density map of the lattice. (d)–(f) Calculated axial electric field (d), transverse electric field (e), and skyrmion number density (f) according to Eq. (1). Here $\lambda = 8.6$ μm, $E_F = 0.65$ eV, and the optimized grating period $\Lambda = 0.305$ μm are adopted. Scale bar: 1 μm.
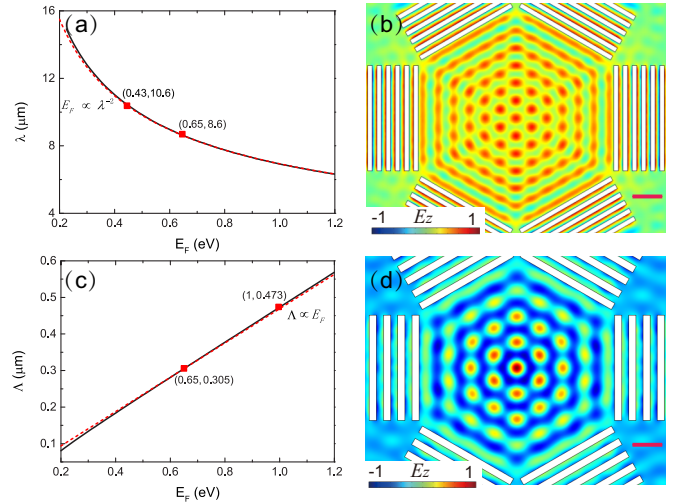

FIG. 3. (a) Relation between the Fermi energies and the wavelength of the incident light for the fixed grating structure. The marks correspond to considered examples in panel (b) and the original case, respectively. (b) Real part of the axial electric field E_z with $E_F = 0.48$ eV and $\Lambda = 0.305$ μm at $\lambda = 10.6$ μm. (c) Relation between the Fermi energies and the period of gratings Λ for the fixed incident wavelength λ. The marks correspond to considered examples in panel (d) and the original case, respectively. (d) Real part of the axial electric field E_z with $E_F = 1$ eV and $\Lambda = 0.473$ μm at $\lambda = 8.6$ μm. Scale bar: 1 μm. The solid lines indicate the calculated results; for comparison, the approximate formulas $E_F \propto \lambda^{-2}$ and $E_F \propto \Lambda$, respectively, are also shown with broken lines.

the topological texture of the optical skyrmions, the calculated skyrmion number density distribution is shown in Fig. 2(c), and one can find that the density distribution is not bubble type and no domain wall exists between two specific field states. The phenomena are consistent with the phenomena in traditional optical skyrmion lattice [7] because the transverse wave vector $q' \gg k_0$ is always satisfied in graphene plasmons. Calculating the skyrmion number in each lattice site, we reach the result $S = 0.94$ (see Appendix B), thus demonstrating the robustness of the optical skyrmions in graphene sheet. Compared with traditional metallic nanostructures, one of the most important advantages for graphene is its tunability. The Fermi energy of the graphene can be tuned dynamically by the back gate voltage V through $E_F = \hbar v_F \sqrt{n\pi} \propto \sqrt{n} \propto \sqrt{V}$; therefore, it enables us to achieve graphene plasmon skyrmions for a broadband frequency by tuning the bias voltage. When tuning the Fermi energy, one can conclude an implicit relationship $f(\Lambda, E_F, \lambda, \bar{\epsilon}) = 0$ without considering the dispersion of silica, where the effective dielectric permittivities $\bar{\epsilon}$ depend on the duty cycle and the ridge height h_0. Here $\bar{\epsilon}$ are fixed both in grating regions and in free propagating regions; one has $f(\Lambda, E_F, \lambda) = 0$. There are two ways to fulfill the relationship. The first way is to keep the grating structure unchanged; the optimized Λ and λ_p can be kept unchanged if $\text{Im}\{\hat{\sigma}(\lambda, E_F)\}\lambda = 0.56$ μm is fixed. At this time, the plasmon wavelength λ_p^0 in the free propagation region also remains unchanged, which means that the properties of graphene plasmon skyrmions remain unchanged as well. Therefore, the designed structure can realize skyrmions in broadband. The explicit relationship $\lambda = \lambda(E_F)|_{\Lambda=0.305\,\mu\text{m}}$ for broadband graphene plasmon skyrmions is shown in Fig. 3(a). When ignoring the graphene conductivity originating from interband transition, the expression may be simplified as $E_F \propto \lambda^{-2}$ [43]. Specifically, the calculated axial field distribution at the selected point (0.43 eV, 10.6 μm) is shown in Fig. 3(b). The lattice parameter a is 518 nm, and the field distribution is almost entirely consistent with Fig. 2(a). The second way is to keep the incident wavelength λ unchanged; then the

optimized Λ can be calculated by $\Lambda/\text{Im}\{\hat{\sigma}(E_F)\} = 4.7$ μm. The explicit relationship between Λ and E_F for graphene plasmon skyrmions is shown in Fig. 3(c). Similarly, the expression can be simplified as $\Lambda \propto E_F$ without considering the interband conductivity. At this moment, the period of graphene plasmon skyrmions is also changed with the tuning of E_F. For example, the calculated field distribution at the selected point (1.0 eV, 0.473 μm) is shown in Fig. 3(d). The lattice parameter a is about 770 nm, which means that each graphene plasmonic skyrmion has a larger unit cell than before. Here the unit cell of skyrmions satisfy $\frac{A(1.0)}{A(0.65)} = [\frac{\lambda_p^0(1.0)}{\lambda_p^0(0.65)}]^2 \approx [\frac{\Lambda(1.0)}{\Lambda(0.65)}]^2 \approx 1.5^2$. Inherent losses are very important to examine the robustness of the topological properties of the plasmonic skyrmions. Because losses will distort the unit vector $\hat{\mathbf{e}}$ and create an unwanted phase difference between electric field components. Fortunately, due to the relatively high-quality factor of graphene plasmons, the real part of the electric field still yields a well-defined skyrmion lattice. However, in this regime, the skyrmion number S for unit cells deviates from unity due to the lattice translation symmetry breaking. There are a lot of damping pathways of GPs, for instance, the GPs can decay via electron-electron scattering γ_{ee}, inelastic scattering with acoustic phonons γ_A, and intervalley electron-phonon scattering γ_K. The total relaxation time satisfies $\tau^{-1} \approx \gamma_{ee} + \gamma_A + \gamma_K$. To demonstrate the influence of the losses on the plasmonic skyrmions, we plot the dependence of the axial electric field E_z on the different relaxation times τ in Fig. 4. One can find that plasmonic skyrmions can hardly be
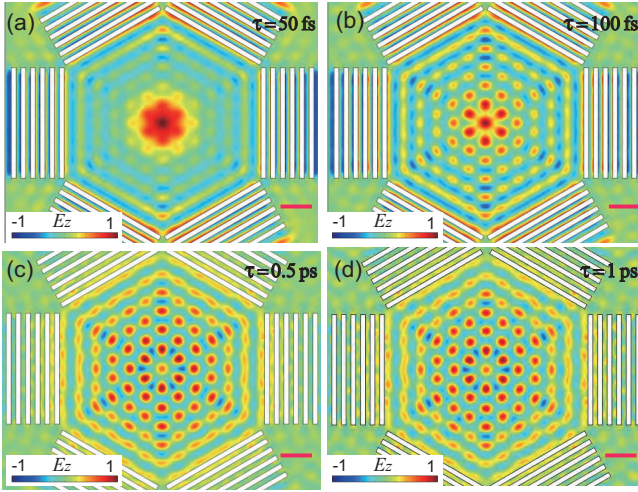
FIG. 4. Real part of the axial electric field E_z for the relaxation times $\tau = 50$ fs, 100 fs, 0.5 ps, and 1 ps, respectively. Scale bar: 1 μm.

FIG. 5. (a)–(e) Real part of the axial electric field E_z excited by RPBs, APBs, x-polarized LPBs, L-CPBs, and R-CPBs, respectively. Scale bar: 1 μm. The insets in panels (a) and (e) show the vector representation of the electric field near the center. (f) Relationship between the intensity of the axial component $|E_z|^2$ excited by RPBs and R-CPBs and the beam waist radius w_0. The electric field in (f) is taken from the limit point just above the origin of the coordinate plane.

distinguished for $\tau \lesssim 50$ fs, when τ reaches more than 100 fs, it is easy to observe the skyrmion lattice in the system. If τ is greater than 0.5 ps, the field distribution will not change significantly. The field distribution at this time is not totally consistent with the analytical results shown in Fig. 2(d), which is due to diffraction and some unwanted reflection from the gratings and boundaries in the system.

Finally, we consider the influence of the states of polarization on the skyrmions' excitation. To facilitate comparison, synthesized doughnut modes with the same intensity distribution are adopted for all of the incident states of polarization. Noticing that $HG_{10} = \frac{\sqrt{2}E_0^{inc}}{w_0} x \exp\left(-\frac{\rho^2}{w_0^2}\right)$ and $HG_{01} = \frac{\sqrt{2}E_0^{inc}}{w_0} y \exp\left(-\frac{\rho^2}{w_0^2}\right)$, the electric field of RPBs, APBs, x-polarized linearly polarized beams (LPBs), and CPBs can be superimposed as

$$
\begin{aligned}
\mathbf{E}_{RPBs} &= HG_{10}\hat{\mathbf{e}}_x + HG_{01}\hat{\mathbf{e}}_y, \\
\mathbf{E}_{APBs} &= -HG_{01}\hat{\mathbf{e}}_x + HG_{10}\hat{\mathbf{e}}_y, \\
\mathbf{E}_{LPBs} &= (HG_{10} + iHG_{01})\hat{\mathbf{e}}_x, \\
\mathbf{E}_{CPBs} &= \frac{1}{\sqrt{2}}(HG_{10} + iHG_{01})(\hat{\mathbf{e}}_x \pm i\hat{\mathbf{e}}_y),
\end{aligned}
\tag{7}
$$

where $\pm$ denote left-circularly/right-circularly polarized beams. The axial electric component E_z excited by RPBs and APBs are depicted in Figs. 5(a) and 5(b), respectively. One can clearly find that skyrmions can hardly be excited by APBs, this is because the polarization direction of the APBs is perpendicular to the periodic directions of the gratings, which can hardly excite the propagating graphene plasmons. Next, the axial component E_z excited by LPBs, L-CPBs, and R-CPBs are depicted in Figs. 5(c)–5(e), respectively. To analyze the excitation mechanism by LPBs and CPBs, we first introduce radial and azimuthal unit vectors as $\hat{\mathbf{e}}_\rho = \hat{\mathbf{e}}_x \cos\phi + \hat{\mathbf{e}}_y \sin\phi$ and $\hat{\mathbf{e}}_\phi = -\hat{\mathbf{e}}_x \sin\phi + \hat{\mathbf{e}}_y \cos\phi$, respectively; thus one has $\hat{\mathbf{e}}_x = \hat{\mathbf{e}}_\rho \cos\phi - \hat{\mathbf{e}}_\phi \sin\phi$ and $\hat{\mathbf{e}}_x \pm i\hat{\mathbf{e}}_y = (\hat{\mathbf{e}}_\rho \pm i\hat{\mathbf{e}}_\phi)\exp(\pm i\phi)$, and incidentally, the phase factor $\exp(\pm i\phi)$ is the reason why the
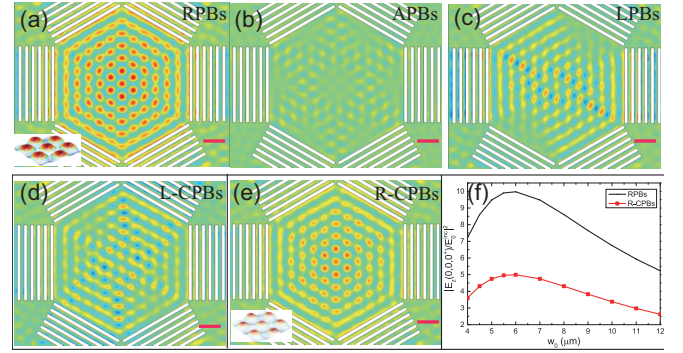
extra displacement of the gratings has to be introduced for the original circularly polarized beams' excitation. Noticing that only the radial component contributes to skyrmions' excitation, one can rewrite the *effective* electric field distribution of RPBs, LPBs, and CPBs as

$$
\begin{aligned}
\tilde{\mathbf{E}}_{RPBs} &= |LG_{01}|\hat{\mathbf{e}}_\rho, \\
\tilde{\mathbf{E}}_{LPBs} &= LG_{01}\hat{\mathbf{e}}_\rho \cos\phi, \\
\tilde{\mathbf{E}}_{CPBs} &= \frac{1}{\sqrt{2}}LG_{01}\hat{\mathbf{e}}_\rho \exp(\pm i\phi).
\end{aligned}
\tag{8}
$$

With $LG_{01} = |LG_{01}|\exp(i\phi)$, one can obtain

$$
\begin{aligned}
\tilde{\mathbf{E}}_{LPBs} &= |LG_{01}|\hat{\mathbf{e}}_\rho \cos\phi \exp(i\phi), \\
\tilde{\mathbf{E}}_{L\text{-}CPBs} &= \frac{1}{\sqrt{2}}|LG_{01}|\hat{\mathbf{e}}_\rho \exp(2i\phi), \\
\tilde{\mathbf{E}}_{R\text{-}CPBs} &= \frac{1}{\sqrt{2}}|LG_{01}|\hat{\mathbf{e}}_\rho.
\end{aligned}
\tag{9}
$$

One can clearly find that LPBs and L-CPBs possess extra phase factors $\exp(i\phi)$ and $\exp(2i\phi)$, respectively, and this is why LPBs and L-CPBs do not excite the skyrmions in Figs. 5(c) and 5(d), while R-CPBs can excite the skyrmions with half the excitation efficiency in terms of intensity as shown in Fig. 5(e). Lastly, the beam waist radius w_0 can also affect the excitation efficiency. Considering that the center of the structure is the position where the interference is always constructive, one can describe the excitation efficiency of the skyrmions by the induced electromagnetic field near this point. The intensity of the axial component $|E_z|^2$ excited by RPBs and R-CPBs as a function of the beam waist radius w_0 is shown in Fig. 5(f). It can be seen that, with the increase of w_0, the excitation efficiency first increases and then decreases, and its peak appears at 6 μm. More importantly, The intensity of the axial component $|E_z|^2$ excited by RPBs is exactly twice as much as that excited by R-CPBs, as expected.

IV. CONCLUDING REMARKS

Looking toward to an experimental observation of our work, one can obtain the RPBs by superposition of two orthogonal linearly polarized light beams TEM_{10} and TEM_{01} via placing some additional optical elements [44] or employing a Nd:YVO4 rod-based master as a laser medium in the laser resonator [45], or by applying space-variant subwavelength gratings [46]. Moreover, if the beam waist radius w_0 is large compared with the propagation distance of GPs, one can use a focus prism or a Fresnel lens to focus the incident light into the grating regions. The silica substrate with six gratings can be fabricated by focused ion beam etching or electron-beam lithography in conjunction with reactive ion etching. Graphene sheets can be obtained by mechanical cleavage from bulk graphite and then transferred to a SiO_2 (300 nm)/Si substrate. The whole graphene film has uniform Fermi energy and does not require microstructure processing, which makes tunability of the Fermi energy of the active graphene flexible in practice. Plasmonic fields are probed point by point using various techniques, such as SNOM [7,47], photoemission electron microscopy [48], or photo-induced force microscopy [49].

In conclusion, we have shown that tunable graphene plasmonic skyrmion lattice in high-quality graphene can be effectively generated by radially polarized light with diffractive gratings. The formed skyrmion lattices have a lattice constant of $a = \frac{2}{\sqrt{3}}\lambda_p^0$ and a deep-subwavelength unit cell area as small as $A \approx 0.0042\lambda^2$. Furthermore, graphene plasmonic skyrmions with identical field distribution at different excited frequencies can be achieved by tuning the Fermi energies without reoptimizing the grating structures, and the unit cell size of plasmonic skyrmion lattice can also be actively tuned by Fermi energies at fixed excited frequencies. Moreover, the plasmonic skyrmions can hardly be distinguished for relaxation times τ shorter than 50 fs. Besides, we find that none of the azimuthal polarized beams, synthesized doughnut linearly polarized beams, or synthesized doughnut left-circularly polarized beams can excite plasmonic skyrmion lattice without shifting the gratings, while radially polarized beams and right-circularly polarized beams can excite plasmonic skyrmion lattice in the axial structure, and the excitation efficiency of plasmonic skyrmion lattice excited by radially polarized beams is exactly twice as much as that excited by right-circularly polarized beams.
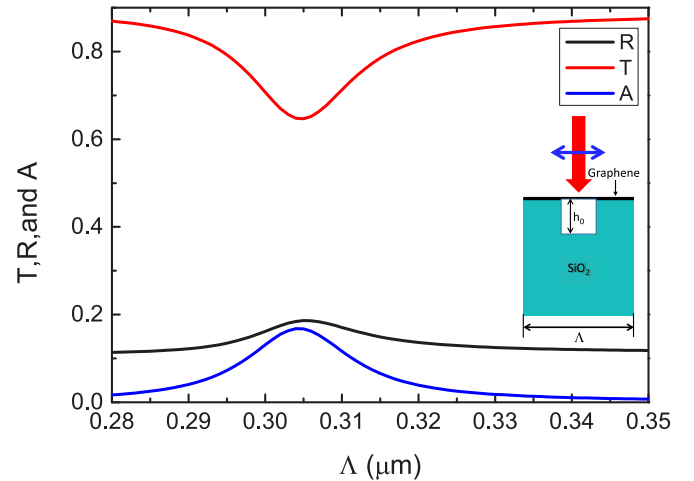
FIG. 6. Dependence of the transmission (T), reflection (R), and absorption (A) on the grating period Λ.

APPENDIX A

A 2D unit cell model of the grating shown in Fig. 6 was investigated by COMSOL MULTIPHYSICS software to achieve the optimized grating period. Figure 6 describes the transmission (T), the reflection (R), and the absorption (A) versus the grating period Λ at normal incidence. Based on Eq. (9) with $\theta = 0$ and $m = 1$, one can find the optimized grating period Λ is 305 nm.

APPENDIX B

In an optical cycle T, the skyrmion number S as a function of time t is shown in Fig. 7. For an appreciable fraction of the first half of the optical cycle, $S \approx -1$. During the second half of the cycle, $S \approx 1$, corresponding to a reverse winding of the graphene plasmonic vectors across the surface.
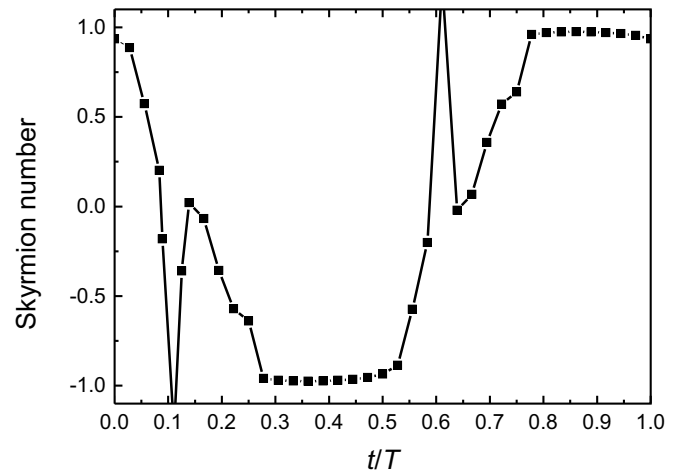

FIG. 7. Dependence of the skyrmion number S on the normalized time t/T.

[1] T. H. R. Skyrme, A unified field theory of mesons and baryons, Nucl. Phys. **31**, 556 (1962).

[2] B. Göbel, I. Mertig, and O. A. Tretiakov, Beyond skyrmions: Review and perspectives of alternative magnetic quasiparticles, Phys. Rep. **895**, 1 (2021).

[3] X. Z. Yu, Y. Onose, N. Kanazawa, J. H. Park, J. H. Han, Y. Matsui, N. Nagaosa, and Y. Tokura, Real-space observation of a two-dimensional skyrmion crystal, Nature (London) **465**, 901 (2010).

[4] S. Parkin and S.-H. Yang, Memory on the racetrack, Nat. Nanotechnol. **10**, 195 (2015).

[5] G. Yu, P. Upadhyaya, Q. Shao, H. Wu, G. Yin, X. Li, C. He, W. Jiang, X. Han, P. K. Amiri, and K. L. Wang, Room-temperature skyrmion shift device for memory application, Nano Lett. **17**, 261 (2017).

[6] Y. Shen, Q. Zhang, P. Shi, L. Du, X. Yuan, and A. V. Zayats, Optical skyrmions and other topological quasiparticles of light, Nat. Photonics **18**, 15 (2024).

[7] S. Tsesses, E. Ostrovsky, K. Cohen, B. Gjonaj, N. H. Lindner, and G. Bartal, Optical skyrmion lattice in evanescent electromagnetic fields, Science **361**, 993 (2018).

[8] T. J. Davis, D. Janoschka, P. Dreher, B. Frank, F.-J. M. zu Heringdorf, and H. Giessen, Ultrafast vector imaging of plasmonic skyrmion dynamics with deep subwavelength resolution, Science **368**, eaba6415 (2020).

[9] L. Du, A. Yang, A. V. Zayats, and X. Yuan, Deep-subwavelength features of photonic skyrmions in a confined electromagnetic field with orbital angular momentum, Nat. Phys. **15**, 650 (2019).

[10] Y. Shen, Y. Hou, N. Papasimakis, and N. I. Zheludev, Supertoroidal light pulses as electromagnetic skyrmions propagating in free space, Nat. Commun. **12**, 5891 (2021).

[11] Q. Zhang, Z. Xie, L. Du, P. Shi, and X. Yuan, Bloch-type photonic skyrmions in optical chiral multilayers, Phys. Rev. Res. **3**, 023109 (2021).

[12] Q. Zhang, Z. Xie, P. Shi, H. Yang, H. He, L. Du, and X. Yuan, Optical topological lattices of Bloch-type skyrmion and meron topologies, Photonics Res. **10**, 947 (2022).

[13] Y. Shen, Topological bimeronic beams, Opt. Lett. **46**, 3737 (2021).

[14] C. Liu, S. Zhang, S. A. Maier, and H. Ren, Disorder-induced topological state transition in the optical skyrmion family, Phys. Rev. Lett. **129**, 267401 (2022).

[15] Y. Shen, E. C. Martínez, and C. Rosales-Guzmán, Generation of optical skyrmions with tunable topological textures, ACS Photonics **9**, 296 (2022).

[16] T. Low and P. Avouris, Graphene plasmonics for terahertz to mid-infrared applications, ACS Nano **8**, 1086 (2014).

[17] A. Grigorenko, M. Polini, and K. Novoselov, Graphene plasmonics, Nat. Photonics **6**, 749 (2012).

[18] F. J. García de Abajo, Graphene plasmonics: challenges and opportunities, ACS Photonics **1**, 135 (2014).

[19] Z. Sun and H. Chang, Graphene and graphene-like two-dimensional materials in photodetection: mechanisms and methodology, ACS Nano **8**, 4133 (2014).

[20] D. Rodrigo, O. Limaj, D. Janner, D. Etezadi, F. J. García de Abajo, V. Pruneri, and H. Altug, Mid-infrared plasmonic biosensing with graphene, Science **349**, 165 (2015).

[21] L. Zundel and A. Manjavacas, Spatially resolved optical sensing using graphene nanodisk arrays, ACS Photonics **4**, 1831 (2017).

[22] A. Y. Nikitin, P. Alonso González, Vélez, Mastel, Centeno, Pesquera, Zurutuza, Casanova, L. E. Hueso, F. H. L. Koppens, and Hillenbrand, Real-space mapping of tailored sheet and edge plasmons in graphene nanoresonators, Nat. Photonics **10**, 239 (2016).

[23] W. Luo, W. Cai, Y. Xiang, W. Wu, B. Shi, X. Jiang, N. Zhang, M. Ren, X. Zhang, and J. Xu, In-plane electrical connectivity and near-field concentration of isolated graphene resonators realized by ion beams, Adv. Mater. **29**, 1701083 (2017).

[24] V. W. Brar, M. S. Jang, M. Sherrott, J. J. Lopez, and H. A. Atwater, Highly confined tunable mid-infrared plasmonics in graphene nanoresonators, Nano Lett. **13**, 2541 (2013).

[25] S. Thongrattanasiri, F. H. L. Koppens, and F. J. García de Abajo, Complete optical absorption in periodically patterned graphene, Phys. Rev. Lett. **108**, 047401 (2012).

[26] S. Kim, M. S. Jang, V. W. Brar, K. W. Mauser, L. Kim, and H. A. Atwater, Electronically tunable perfect absorption in graphene, Nano Lett. **18**, 971 (2018).

[27] M. Polini, Tuning terahertz lasers via graphene plasmons, Science **351**, 229 (2016).

[28] S. Chakraborty, O. P. Marshall, T. G. Folland, Y. J. Kim, A. N. Grigorenko, and K. S. Novoselov, Gain modulation by graphene plasmons in aperiodic lattice lasers, Science **351**, 246 (2016).

[29] C. Bai, J. Chen, Y. Zhang, D. Zhang, and Q. Zhan, Dynamic tailoring of an optical skyrmion lattice in surface plasmon polaritons, Opt. Express **28**, 10320 (2020).

[30] R. Dorn, S. Quabis, and G. Leuchs, Sharper focus for a radially polarized light beam, Phys. Rev. Lett. **91**, 233901 (2003).

[31] Y. I. Salamin, Mono-energetic gev electrons from ionization in a radially polarized laser beam, Opt. Lett. **32**, 90 (2007).

[32] Q. Zhan, Trapping metallic rayleigh particles with radial polarization, Opt. Express **12**, 3377 (2004).

[33] T. Kuga, Y. Torii, N. Shiokawa, T. Hirano, Y. Shimizu, and H. Sasada, Novel optical trap of atoms with a doughnut beam, Phys. Rev. Lett. **78**, 4713 (1997).

[34] S. Roy, K. Ushakova, Q. van den Berg, S. F. Pereira, and H. P. Urbach, Radially polarized light for detection and nanolocalization of dielectric particles on a planar substrate, Phys. Rev. Lett. **114**, 103903 (2015).

[35] L. Novotny, M. R. Beversluis, K. S. Youngworth, and T. G. Brown, Longitudinal field modes probed by single molecules, Phys. Rev. Lett. **86**, 5251 (2001).

[36] A. Yanai, M. Grajower, G. M. Lerman, M. Hentschel, H. Giessen, and U. Levy, Near- and far-field properties of plasmonic oligomers under radially and azimuthally polarized light excitation, ACS Nano **8**, 4969 (2014).

[37] B. Wunsch, T. Stauber, F. Sols, and F. Guinea, Dynamical polarization of graphene at finite doping, New J. Phys. **8**, 318 (2006).

[38] E. H. Hwang and S. Das Sarma, Dielectric function, screening, and plasmons in two-dimensional graphene, Phys. Rev. B **75**, 205418 (2007).

[39] V. P. Gusynin, S. G. Sharapov, and J. P. Carbotte, Unusual microwave response of Dirac quasiparticles in graphene, Phys. Rev. Lett. **96**, 256802 (2006).

[40] A. A. Tovar, Production and propagation of cylindrically polarized Laguerre–Gaussian laser beams, J. Opt. Soc. Am. A **15**, 2705 (1998).

[41] Q. Zhan, Cylindrical vector beams: from mathematical concepts to applications, Adv. Opt. Photonics **1**, 1 (2009).

[42] D. Deng and Q. Guo, Analytical vectorial structure of radially polarized light beams, Opt. Lett. **32**, 2711 (2007).

[43] C. Guan, T. Yuan, R. Chu, Y. Shen, Z. Zhu, J. Shi, P. Li, L. Yuan, and G. Brambilla, Generation of ultra-wideband achromatic airy plasmons on a graphene surface, Opt. Lett. **42**, 563 (2017).

[44] S. C. Tidwell, D. H. Ford, and W. D. Kimura, Generating radially polarized beams interferometrically, Appl. Opt. **29**, 2234 (1990).

[45] Y. Kozawa and S. Sato, Generation of a radially polarized laser beam by use of a conical Brewster prism, Opt. Lett. **30**, 3063 (2005).

[46] Z. Bomzon, G. Biener, V. Kleiner, and E. Hasman, Radially and azimuthally polarized beams generated by space-variant dielectric subwavelength gratings, Opt. Lett. **27**, 285 (2002).

[47] P. Alonso-González, A. Y. Nikitin, F. Golmar, A. Centeno, A. Pesquera, S. Vélez, J. Chen, G. Navickaite, F. Koppens, A. Zurutuza, F. Casanova, L. E. Hueso, and R. Hillenbrand, Controlling graphene plasmons with resonant metal antennas and spatial conductivity patterns, Science **344**, 1369 (2014).

[48] G. Spektor, D. Kilbane, A. K. Mahro, B. Frank, S. Ristok, L. Gal, P. Kahl, D. Podbiel, S. Mathias, H. Giessen, F. J. Meyer Zu Heringdorf, M. Orenstein, and M. Aeschlimann, Revealing the subfemtosecond dynamics of orbital angular momentum in nanoplasmonic vortices, Science **355**, 1187 (2017).

[49] A. Ambrosio, M. Tamagnone, K. Chaudhary, L. A. Jauregui, P. Kim, W. L. Wilson, and F. Capasso, Selective excitation and imaging of ultraslow phonon polaritons in thin hexagonal boron nitride crystals, Light Sci. Appl. **7**, 27 (2018).